

**BONE MINERAL DENSITY DETERMINATION
USING DIGITAL RADIOGRAPHY**

BONE MINERAL DENSITY DETERMINATION

USING DIGITAL RADIOGRAPHY

By

MICHELLE JEANNE COTTREAU, B.Sc.

A Project

Submitted to the School of Graduate Studies

in Partial Fulfilment of the Requirements

for the Degree

Master of Science

(Health and Radiation Physics)

McMaster University

October 1993

MASTER OF SCIENCE (1993)

MCMASTER UNIVERSITY

(Health and Radiation Physics)

Hamilton, Ontario

TITLE: Bone Mineral Density Determination Using
Digital Radiography

AUTHOR: Michelle Jeanne Cottreau, B.Sc. (U.P.E.I.)

SUPERVISOR: Dr. Colin Webber

NUMBER OF PAGES: xi, 73

ABSTRACT

There is a need for an improved bone mineral density measurement procedure for neonates. Currently, measurements are made using single photon absorptiometry (SPA). The poor reproducibility of this method means that it has little direct clinical diagnostic application and is therefore not suitable for diagnosing disease in individual patients.

A technique using digital radiography has been developed to measure bone mineral density. Digital images of phantoms and chicken bones were acquired at two kvp settings of a digital angiographic unit. Digital information from water, aluminum and lucite phantoms were used to calculate effective mass attenuation coefficients of the phantom materials. These values were subsequently used in bone mineral density calculations of sections of the chicken bones.

The bone mineral densities of the chicken bones obtained from the digital radiography method were

compared to SPA measurements. The digital radiography method gave consistently higher bone mineral densities for the bones than SPA. This could be due to the differences in measurement technique as SPA scans a single slice whereas digital radiography images a large area of the bone.

ACKNOWLEDGEMENTS

I would like to thank my supervisor, Dr. Colin Webber, for his encouragement and guidance during the course of my research.

I would also like to express my gratitude to the Radiology Department for the use of the angiography unit and to those who taught me to use it and the Display program. I would also like to thank Chris Gordon and Lesley Chambers for making it a pleasure to come to work each day.

Most importantly, I owe the successful completion of this project report to my husband, Bill. His support and helpful suggestions were much appreciated and his never ending words of encouragement (or subtle threats) helped me to finally finish.

TABLE OF CONTENTS

	<u>Page</u>
CHAPTER 1 INTRODUCTION	
1.1 Clinical Rationale.....	1
1.2 Single Photon Absorptiometry.....	2
1.3 Other Methods.....	4
1.4 Digital Radiography.....	5
1.5 Scope of Project.....	6
CHAPTER 2 THEORY	
2.1 X-ray Production.....	8
2.2 X-ray Interaction With Matter.....	10
2.3 X-ray Attenuation.....	15
2.4 Single Photon Absorptiometry.....	18
CHAPTER 3 MATERIALS AND METHODS	
3.1 Apparatus.....	21
3.1.1 The Generation of X-rays.....	21
3.1.2 The Imaging System.....	23
3.2 Technique.....	28
3.3 Phantoms.....	29

Table of contents (continued)

	<u>Page</u>
3.3.1 Aluminum Stepwedge.....	29
3.3.2 Water Phantom.....	33
3.3.3 Lucite Phantom.....	33
3.3.4 The Chicken Bones.....	34
3.4 Method.....	35
3.4.1 Acquiring the Digital Images.	35
3.4.2 Accessing the Digital Images.	36
3.4.3 Determination of Mass Attenuation Coefficients.....	38
3.4.4 Determination of BMD.....	40
3.5 Single Photon Absorptiometry (SPA).	40
3.5.1 Calibration of Densitometer..	41
3.5.2 Measurement of BMD.....	41

CHAPTER 4 RESULTS AND DISCUSSION

4.1 SPA Results.....	44
4.2 Data Analysis.....	44
4.3 Run #1.....	46
4.4 Run #2.....	49
4.5 Run #3.....	52
4.6 Run #4.....	61

Table of contents (continued)

	<u>Page</u>
CHAPTER 5 SUMMARY	68
BIBLIOGRAPHY	71

LIST OF TABLES

	<u>Page</u>
3.1 Mass attenuation coefficients of bone, soft tissue and phantom materials as a function of photon energy.....	32
4.1 Bone mineral densities of fourteen chicken bones using SPA.....	45
4.2 Bone mineral densities of six chicken bones using digital radiography.....	54
4.3 Bone mineral densities of thirteen chicken bones using digital radiography.....	59
4.4 Bone mineral densities of fourteen chicken bones using digital radiography.....	65
4.5 Summary of effective mass attenuation coefficients determined.....	67

LIST OF FIGURES

	<u>Page</u>
3.1 The image intensifier.....	24
3.2 Schematic of the digital angiographic system...	27
3.3 Experimental setup.....	30
3.4 The aluminum stepwedge.....	31
3.5 Experimental setup for the measurement of the chicken bones using SPA.....	42
4.1 Determination of the effective mass attenuation coefficients of water and aluminum by linear regression of equation 3.1.....	47
4.2 Digital images of the chicken bones in the lucite phantom.....	50
4.3 Determination of the effective mass attenuation coefficients of water and aluminum by linear regression of equation 3.1.....	51
4.4 Determination of the effective mass attenuation coefficients of lucite by linear regression of equation 3.2.....	53
4.5 Comparison of the bone mineral densities of five chicken bones obtained by digital radiography and SPA.....	55
4.6 Determination of the effective mass attenuation coefficients of water and aluminum by linear regression of equation 3.1.....	57

List of figures (continued)

	<u>Page</u>
4.7 Determination of the effective mass attenuation coefficients of lucite by linear regression of equation 3.2.....	58
4.8 Comparison of the bone mineral densities of thirteen chicken bones obtained by digital radiography and SPA.....	60
4.9 Determination of the effective mass attenuation coefficients of water and aluminum by linear regression of equation 3.1.....	62
4.10 Determination of the effective mass attenuation coefficients of lucite by linear regression of equation 3.2.....	64
4.11 Comparison of the bone mineral densities of thirteen chicken bones obtained by digital radiography and SPA.....	66

Chapter 1 Introduction

1.1 Clinical Rationale

The measurement of bone mineral content in neonatal patients is useful for examining disorders of bone mineralization which are common in premature infants (Steichen et al 1980). Very low birth weight infants have the greatest risk for developing bone mineralization defects (Koo et al 1986). Measurement of bone mineral content at birth in infants of different gestational ages has been done to determine the normal rate of bone mineralization. Long term studies have shown that extrauterine bone mineralization in many preterm infants lags behind normal intrauterine mineralization (Vymeister et al 1987). Due to the improvements in neonatal intensive care the survival rates of very premature infants have increased. As a result, the incidence of rickets of prematurity has increased (James et al 1986).

Measuring bone mineral content can provide the physician or researcher with information regarding skeletal growth and mineralization and will help determine the effectiveness of experimental treatments.

1.2 Single Photon Absorptiometry

Currently bone mineral measurements in neonates are obtained using the technique of single photon absorptiometry (SPA). SPA was first described by Cameron and Sorenson (1963) and was later modified for use in babies (Steichen et al 1978).

There has been a number of published studies where SPA has been used to investigate the bone mineral content in infants (Greer et al 1983, Tyson et al 1983, James et al 1986, Vyhmeister et al 1987 and 1988). Though some of these studies claim that precise and reproducible measurements can be made with SPA, there are inherent difficulties with the method. In one study the bone densitometer failed to detect the bone edge for 40 % of the infants (Tyson et al 1983). This was presumed to be due to either large apparatus variability or a very low bone mineral content. They also showed

that between successive scans in the same infant, the variability was large (- 73 % to + 63 %) where the major source of variability was due to the densitometer itself. They concluded that commercially available densitometers were unreliable for evaluating bone mineralization in preterm infants. In another study, using a commercially available densitometer modified for use in infants, it was found that the modified unit was still not able to detect bone edges in 32.5 % of the infants measured (Vyhmeister et al 1987).

Current investigations of bone mineral content using SPA require long term studies containing large numbers of subjects in order to obtain statistically significant results (Hansen 1988). One difficulty with SPA that contributes significantly to the reproducibility and precision of the method is patient movement during the measurement. Commercial absorptiometers are equipped with immobilization devices which help to restrict arm movement during the measurement but it is not always adequate for complete immobility of a premature infants arm for the duration of a scan (Steichen 1988). Another major error source is

the location and relocation of the scan site (Steichen et al 1988). The reproducibility of SPA depends primarily on precise repositioning of the infant. It has been reported that the coefficient of variation for repositioning error was 12.1 % for individual scans (Vyhmeister et al 1987).

Despite the various problems with SPA, it is still regarded by investigators as a useful tool for measuring bone mineral content. Presently, though, SPA has little direct clinical diagnostic application and is therefore not suitable for diagnosing disease in individual infants (Steichen et al 1988).

1.3 Other Methods

Bone mass measurements are also made by a number of other methods. Dual photon absorptiometry (DPA) is used primarily for measuring hip and lumbar spine bone mineral density in adults. The large beam size and longer scan times would make this method unsuitable for forearm measurements in preterm infants. Dual x-ray absorptiometry uses x-rays instead of a radionuclide source as in SPA or DPA. This method has shorter scan

times, better spatial resolution and improved precision over DPA but the scan times are still significant. Quantitative computed tomography (QCT) has worse precision and accuracy than SPA or DPA (Barden et al 1988). The high radiation dose and long scan times also make this method unsuitable for measurements in neonates.

1.4 Digital Radiography

The use of digital radiography for bone mineral measurements in neonates was first suggested by Hawkes et al (1987). X-ray films of the forearm and a lucite and aluminum stepwedge were obtained at 40 and 120 kVp. The films were digitised using an image analysis system. The aluminum and lucite images were used to construct a calibration table to convert the high and low kV images to an aluminum equivalent image. The aluminum image can then be integrated across the shaft of the forearm to produce a plot of bone mineral per unit length of the bone. This technique was used to follow postnatal changes in bone mineralization of the radii of 15 infants of less than 30 weeks gestation (Lyon et al

1989).

The digital radiography method will potentially improve on some of the inherent problems with SPA. The measurement time is very short, a fraction of a second, which will eliminate the problems due to patient movement. The entire radius is imaged so that repositioning errors are also eliminated. The bone mineral density can be determined for any section of the bone or for the whole bone.

1.5 Scope of Project

The scope of this project is to develop a method using digital radiography to measure bone mineral density. Digital radiographic images will be acquired and the digital information will be accessed and used directly. Digital images of aluminum, water and lucite phantoms and chicken bones will be acquired at 120 and 40 kVp. Effective mass attenuation coefficients of the phantom materials will be determined. These values will be used to calculate the bone mineral density of the chicken bones.

The goal of this research is to develop a

clinical procedure to measure bone mineral density in neonates.

Chapter 2 Theory

2.1 X-ray Production

X-rays are a form of ionizing radiation. They are photons with energies ranging from 1 keV to 35 MeV. In the diagnostic energy region, x-ray energies range from 1 keV to 150 keV and are produced by an x-ray tube which is one component of a patient x-ray unit.

The x-ray tube consists of two heated tungsten filaments, a rotating tungsten anode and a high voltage supply all encased in an evacuated glass tube. X-rays are produced when some of the fast-moving electrons from the filament interact with the tungsten target (anode). In most x-ray tubes, approximately 1% of the total electron energy is converted into x-rays. X-ray photons are emitted in all directions but only a small portion of the photons generated actually pass through the tube window and contribute to the useful beam. There are two types of interactions between electrons and the anode

that produce x-rays. The types of x-rays produced are known either as Bremsstrahlung or characteristic radiation.

Bremsstrahlung, a term which comes from the German for "braking radiation", is produced when electrons pass near the nuclei of target atoms. The negatively charged electron is attracted towards the nucleus and is deflected from its original path. The electron may lose energy and be slowed down by this direction change and the lost kinetic energy is emitted directly in the form of an x-ray photon. An electron may undergo many reactions before coming to rest and the initial electron energy may vary widely. This causes a wide distribution in the energy of the radiation produced and a continuous x-ray spectrum is formed.

Characteristic radiation results when the bombarding electrons interact with the orbital electrons of the target atoms. Electrons are ejected from the inner orbits which results in a positively charged atom. To rid itself of excess energy, the atom emits an x-ray photon. If, in a tungsten target, the incoming electron interacts with a K shell electron, characteristic x-rays

of tungsten ($K_{\alpha 1}$ 59.3 keV; $K_{\beta 1}$ 67.2 keV) will be emitted as the K shell vacancy is filled. X-rays will also be generated from transitions involving other electron shells but their energies will be small, producing mostly heat or x-rays that are absorbed in the walls of the x-ray tube.

The x-ray beam is, therefore, composed of a continuous and a characteristic spectrum, superimposed upon each other. The maximum energy of the x-ray spectrum is dependent upon the peak kilovoltage (kVp) used. The kVp is the kilovoltage applied to the x-ray tube to accelerate the electrons released from the filament. The kVp setting is then the maximum x-ray photon energy in kiloelectron volts (keV).

2.2 X-ray Interaction With Matter

When x-ray photons are incident upon matter, one of two things may happen: they may interact with the material or they may pass through without interacting. If an interaction takes place, the photon may either be absorbed during the photoelectric effect, or be scattered by either the coherent or incoherent (Compton)

scattering process. Scattering contributes to the deterioration of the resulting x-ray image. In the diagnostic energy range, the dominant process is Compton scattering by atomic electrons. As photon energy decreases photoelectric absorption becomes increasingly important, especially for high Z elements. The probability of coherent scattering also increases as photon energy decreases.

Photoelectric interactions result in the complete removal of the incident photon from the x-ray beam. The more tightly bound electrons are the important ones in bringing about photoelectric absorption. The incoming photon encounters an electron in an orbital shell and transfers all of its energy. The probability of an interaction is greatest when the incoming photon has just enough energy to eject the bound electron. The probability falls as the photon energy increases above the K absorption edge. The photoelectron is ejected from the atom and is absorbed locally. The electron vacancy is filled by an electron transition from an outer shell which results in emission of characteristic radiation. The energy of characteristic radiation is dependent on

differences between the binding energies of the two electron shells involved which in turn depend upon the atomic number of the atom. The probability of photoelectric effect increases approximately as the cube of the atomic number.

Compton scattering is a process which produces almost all the scatter radiation encountered in diagnostic radiology. When the energy of an incoming photon is very much greater than the binding energy of the electron with which it interacts, Compton scattering can occur. That is, Compton interactions occur with essentially free electrons. For elements of relatively high atomic number only the outer shell electrons can be considered to be free in the diagnostic energy region. In elements with low atomic number (e.g. soft tissue components) all electrons can be considered free. In Compton reactions, an incident photon (E_{γ}) strikes a free outer shell electron, ejecting it from its orbit. The photon is deflected by the electron so that it travels in a new direction. The scattered photon (E'_{γ}) retains part of its original energy with the remainder carried by the recoil electron as kinetic energy (E_e).

where, by conservation of energy,

$$E_{\gamma} = E'_{\gamma} + E_e \quad (2.1)$$

The scattered photon energy is given by

$$E'_{\gamma} = \frac{E_{\gamma}}{1 + \frac{E_{\gamma}}{m_0 c^2} (1 - \cos\theta)} \quad (2.2)$$

where θ is the scattering angle. The recoil electron may then go on to ionize or excite other atoms before coming to rest. From equation (2.2) we can see that at narrow angles of deflection, scattered photons in the diagnostic energy range retain most of their original energy. Such scattered photons are high in energy and are not easily removed by filters and since the angle of deflection is small, they are not efficiently removed by grids. These photons provide no useful information to the radiograph and simply degrade the image. The probability of Compton scattering decreases with increasing photon energy and is almost independent of the atomic number of the medium. The differential cross-section for Compton scattering first calculated by Klein and Nishina takes the form

$$\left(\frac{d\sigma}{d\Omega}\right)_{\text{KN}} = r_e^2 \left(\frac{E'}{E_\gamma}\right)^2 \left[\frac{E'}{E_\gamma} + \frac{E}{E_\gamma'} - \sin^2\theta \right] \quad (2.3)$$

where $r_e = \frac{e^2}{m_e c^2}$ and is defined as the classical electron radius. To a close approximation, the probability of Compton scattering can be expressed as the product of the Klein-Nishina cross-section and the incoherent scattering function, $S(v, Z)$

$$\left(\frac{d\sigma}{d\Omega}\right)_{\text{COM}} = \left(\frac{d\sigma}{d\Omega}\right)_{\text{KN}} S(v, Z) \quad (2.4)$$

The incoherent scattering function represents the probability that an atom will be raised to any excited or ionized state when a photon transfers some momentum to an atomic electron. It takes into account the effect of the electron binding on the total Compton cross-section. The variable v is related to the momentum transfer and is given by

$$v = \frac{1}{\lambda} \sin \frac{\theta}{2} \quad (2.5)$$

where λ is the photon wavelength.

Coherent scattering occurs when a low energy photon interacts with a whole atom. Scattering is a result of the cooperative interaction with all the

electrons of the atom. The atom de-excites, and returns to its ground state, by the emission of a photon. The atom is, therefore, neither ionized or excited and the recoil momentum is absorbed by the entire atom. The photon loses essentially none of its energy and is usually scattered at a small angle. Coherent scattering predominates when low energy photons are scattered in high Z materials and the angle of scatter is greatest at low energies. The differential cross-section for coherent scattering per atom is

$$\left(\frac{d\sigma'}{d\Omega}\right)_{\text{COH}} = \frac{r_0^2}{2} (1 + \cos^2\theta) F^2(v, Z) \quad (2.6)$$

where $F^2(v, Z)$ is the square of the atomic form factor. The atomic form factor is the probability that the Z electrons of the atom take up recoil momentum without absorbing any energy. The net effect of coherent scattering is to deflect the photon.

2.3 X-ray Attenuation

Attenuation is the reduction in the intensity of an x-ray beam as it traverses matter by absorption and scattering of photons. When an x-ray photon in the diagnostic energy region interacts with matter any one

of the three described processes may occur. The probability of each type of interaction is proportional to the cross-section for that process. The total probability of an interaction is then proportional to the sum of cross-sections for all possible interactions. The total probability is called the total linear attenuation coefficient μ_T which is given as

$$\mu_T = \mu_{PE} + \mu_{COM} + \mu_{COH} \quad (2.7)$$

where μ_{PE} , μ_{COM} , μ_{COH} are the linear attenuation coefficients for each interaction process. The linear attenuation coefficient μ is the probability per unit path length for an interaction and is defined as

$$\mu = n_T \sigma \quad (2.8)$$

where σ is the cross-section and n_T is the target density. Therefore, equation (2.7) becomes

$$\mu_T = n_T (\sigma_{PE} + \sigma_{COM} + \sigma_{COH}) \quad (2.9)$$

Using the linear attenuation coefficient we can then define an equation which describes the passage of a photon beam through an object

$$I = I_0 e^{-\mu_T t} \quad (2.10)$$

where I_0 is the initial beam intensity, I is the beam intensity after passage through the object and t is the

thickness of the object. Equation (2.10) can be modified to take into account the density of the object

$$I = I_0 e^{-\left(\frac{\mu}{\rho}\right) T} \quad (2.11)$$

where $\left(\frac{\mu}{\rho}\right)$ is called the mass attenuation coefficient which is simply the linear attenuation coefficient divided by the density of the object and T is the density thickness of the object defined as the thickness multiplied by the density. Since the mass attenuation coefficient varies with photon energy, it will have to be measured in the subsequent experiments. The measured value will be an effective mass attenuation coefficient as a result of the continuous nature of the x-ray spectrum. Therefore, any references to the mass attenuation coefficient will, in fact, refer to the effective mass attenuation coefficient.

Equation (2.11) can be used to describe the transmission of an x-ray beam through an object consisting of bone (B) and soft tissue (T). For each x-ray spectrum, with a maximum energy of kVp_n , there is an equation describing the passage of the beam:

$$\text{kVp}_1: \quad I_1 = I_{o1} e^{-\left[\left(\frac{\mu}{\rho}\right)_{B1} T_B + \left(\frac{\mu}{\rho}\right)_{T1} T_T\right]} \quad (2.12)$$

$$\text{kVp}_2: \quad I_2 = I_{o2} e^{-\left[\left(\frac{\mu}{\rho}\right)_{B2} T_B + \left(\frac{\mu}{\rho}\right)_{T2} T_T\right]} \quad (2.13)$$

The density thickness of bone, more commonly known as bone mineral density (BMD) can be obtained by solving equations (2.12) and (2.13) simultaneously for T_B to get

$$T_B = \frac{\ln \left(\frac{I_1}{I_{o1}} \right) - \mu_R \ln \left(\frac{I_2}{I_{o2}} \right)}{\mu_R \left(\frac{\mu}{\rho} \right)_{B2} - \left(\frac{\mu}{\rho} \right)_{B1}} \quad (2.14)$$

where $\mu_R = \frac{(\mu/\rho)_{T1}}{(\mu/\rho)_{T2}}$ which, from equations (2.12) and

(2.13), is equal to $\frac{\ln (I_o/I)_1}{\ln (I_o/I)_2}$ when T_B is equal to

zero. The above equations are similar to those used in another bone mineral density measuring procedure called dual photon absorptiometry.

2.4 Single Photon Absorptiometry

Single photon absorptiometry (SPA) is a method which uses a radioisotope to measure bone mineral density. This measurement technique requires a thin, but

constant, thickness of soft tissue and bone, so the forearm (radius) is usually the measurement region of choice. A water bag surrounds the measurement site of the forearm to maintain a constant tissue thickness. A 27.5 keV photon beam is produced using a 200 mCi I-125 source. This low energy x-ray is used to maximize the difference in attenuation between bone and tissue. The gamma rays are detected by a NaI(Tl) scintillation detector after transmission through the forearm. The photon beam is narrowly collimated at the source and detector. The number of transmitted photons is counted as the source-detector assembly is scanned across the arm. To obtain BMD two photon transmission measurements are made: one through bone and soft tissue and the other through soft tissue adjacent to the bone. The two equations describing the transmission of the photon beam are similar to those described in section 2.3 and can be written as

$$I = I_0 e^{-\left[\left(\frac{\mu}{\rho}\right)_B T_B + \left(\frac{\mu}{\rho}\right)_T T_{T1}\right]} \quad (2.15)$$

$$I' = I_0 e^{-\left(\frac{\mu}{\rho}\right)_T T_{T2}} \quad (2.16)$$

where I is the beam intensity after passage through bone and soft tissue, I' is the beam intensity after passage through soft tissue alone, and T_{T1} and T_{T2} are the density thicknesses of soft tissue for the first and second measurements, respectively. Equations (2.15) and (2.16) can be manipulated to give an equation for the BMD in units of g/cm^2

$$T_B = \frac{\ln \left(\frac{I'}{I} \right)}{\left(\frac{\mu}{\rho} \right)_B - \left(\frac{\mu}{\rho} \right)_T \left(\frac{\rho_T}{\rho_B} \right)} \quad (2.17)$$

Chapter 3 Materials and Methods

3.1 Apparatus

The equipment used was the clinical angiography unit in the Department of Radiology, McMaster University Medical Centre, Chedoke-McMaster Hospitals.

3.1.1 The Generation of X-Rays

The x-rays were generated using a three phase generator (Maximus CM 120, Philips Medical Systems, Toronto, Ontario) coupled to an x-ray tube (Super Rotalix ROT 500, Philips Medical Systems). Attached to the x-ray tube is a collimator (Model D385072, Philips Medical Systems).

The generator supplies the high voltage potential to the filament and anode in the x-ray tube and regulates the current flow to the filament as well as the duration of the x-ray exposure. On the generator console, the kVp, milliamperes, time and focal spot size

can be selected to vary the x-ray irradiation. The kVp can be varied from 40 to 150. The milliampere (mA) selection is used to vary the filament current in the x-ray tube. The time (s) is the duration of the x-ray exposure. The mA and time can be selected in unison (mAs). The two focal spot sizes are 0.6 mm and 1.2 mm.

The x-rays emitted from the x-ray tube window are in the form of a conical beam. The beam is controlled by the collimator which is fitted to the tube window. The collimator contains two pairs of lead shutters which can be adjusted to produce any square or rectangular x-ray field desired. The lead shutters absorb the section of the beam which has not been selected. The collimator has 1 mm of aluminum and 0.5 mm of niobium filtration added. Both filters absorb low energy x-rays which significantly reduces patient dose with minimal image degradation. The x-ray table top (XRE, Philips Medical Systems) was constructed of carbon fibre with an equivalent absorption of 1.0 mm Al at 80 kVp.

3.1.2 The Imaging System

The imaging system consists of an image intensifier (II), a television camera and a television monitor connected to a digital system.

The input surface of the II (Model G213-017, Philips Medical Systems) is covered with a 36 cm diameter linear grid (Model V5059, Philips Medical Systems). The grid consists of lead strips which are oriented in a plane parallel to the incoming x-rays so that primary radiation passes through. Most scattered radiation will be absorbed by the lead since it will be incident on the grid at an angle. The grid is constructed with the lead strips slightly angled and focused at a line 110 cm away in space. The grid ratio is 10:1 and refers to the ratio between the height of the lead strips and the distance between them.

The II has a 36 cm input diameter and 25 mm output diameter. X-rays entering an image intensifier tube (figure 3.1) are first incident upon a phosphor which absorbs x-ray photons. The input phosphor is a fluorescent screen composed of cesium iodide crystals deposited on a thin substrate. The x-ray energy is

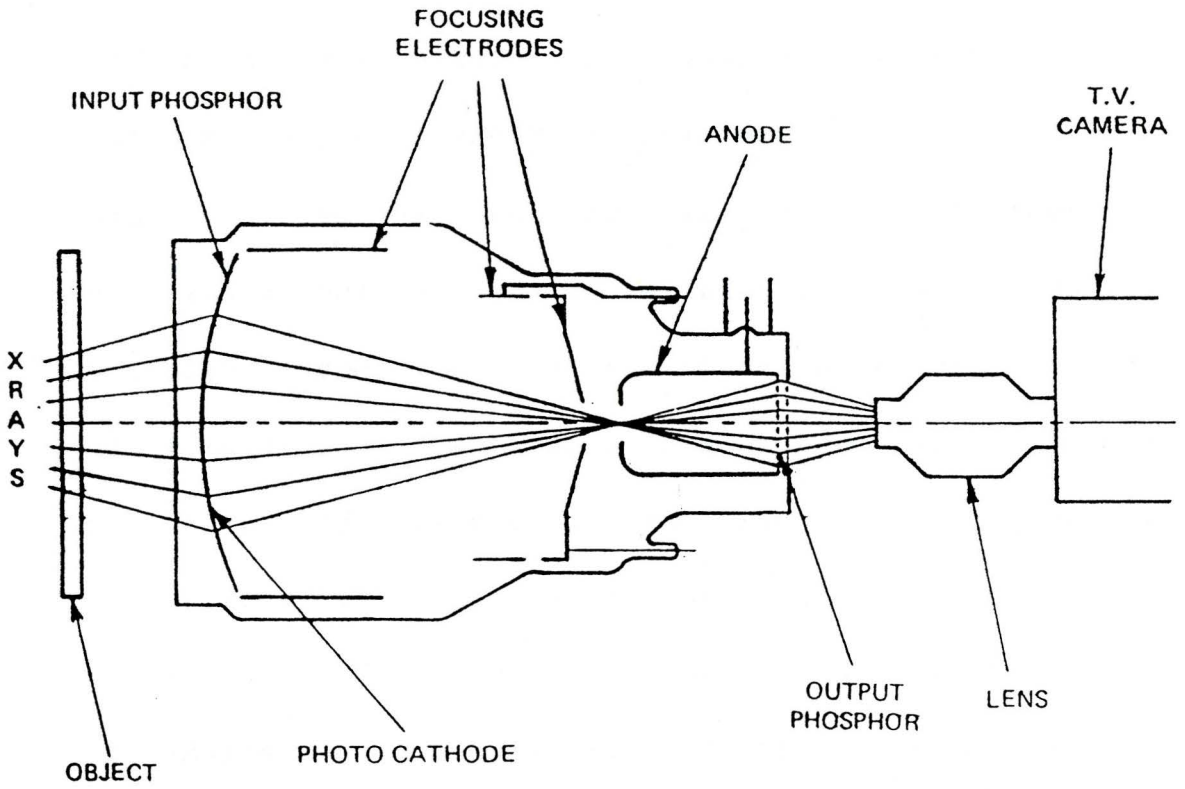


Figure 3.1 The image intensifier.

converted into light photons in proportion to the intensity of the incident x-ray beam. The light photons are then incident upon a photocathode which emits electrons in proportion to the intensity of the light. An anode is located at the other end of the II to accelerate the electrons towards the output phosphor. Electrostatic lenses are used to focus the electron beam as it flows towards the anode. The electrons pass through a common focal point so that the image is inverted when they reach the output phosphor. The input phosphor is curved to prevent distorted focussing as it allows all regions of the electron beam to travel the same distance to the output phosphor. The output phosphor is comprised of a thin aluminum layer which covers a layer of zinc cadmium sulfide. The aluminum will prevent light from traveling back through the II and activating the photocathode. The image on the output phosphor is reduced in size which causes the image to be brighter. The image formed at the output phosphor is then scanned by a TV camera.

The TV camera (Techcam, General Electric Medical Systems, Mississauga, Ontario) uses a plumbicon

television tube and is part of a closed circuit system which also includes a monitor and camera control unit. The TV camera converts the light signal from the output phosphor of the II into a series of electronic pulses. The amplitude of the electronic or video signal is directly proportional to the number of x-rays exiting the object being imaged. The video signal can be sent to the monitor for direct viewing or be sent to the ADC. The ADC, or analog to digital converter, is the main device incorporated into the digital angiographic system (Technicare DR 960 High Speed Disk System, General Electric Medical Systems, Mississauga, Ontario) which converts the analog signal of the x-ray image to a digital signal after it has been scanned by the TV camera. The digital signal is comprised of a series of binary values which are then translated into pixel values to form the digital image viewed on the monitor. The digital images can also be archived to magnetic tape for later viewing. A block diagram of the digital angiography system used is shown in figure 3.2.

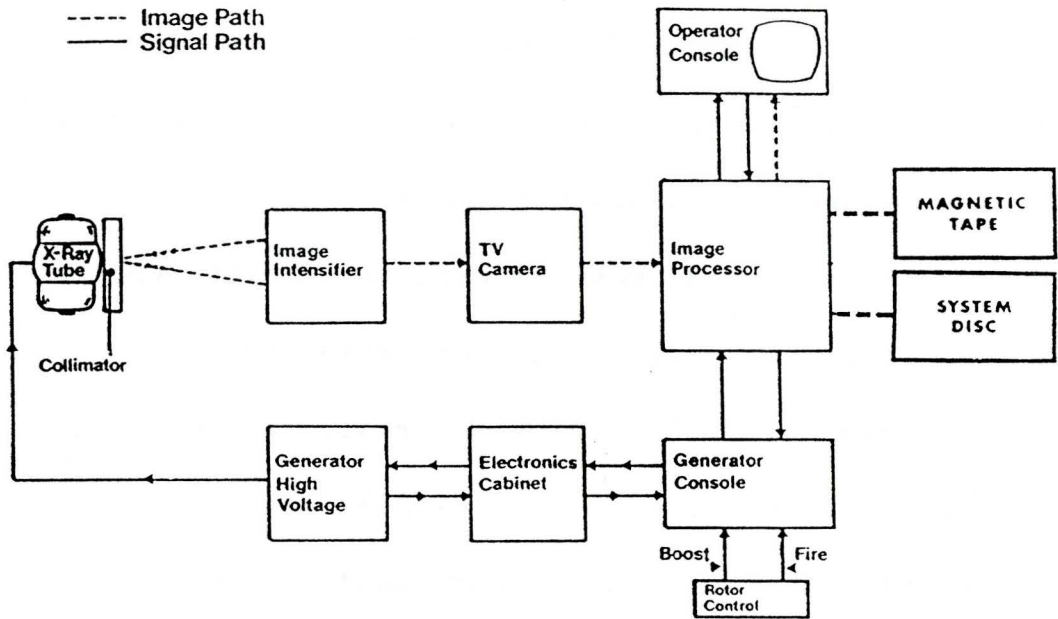


Figure 3.2 Schematic of the digital angiographic system.

3.2 Technique

Images were acquired at two distinct settings of the x-ray generator which were 40 kVp and 120 kVp. The accuracy of the kVp was verified through quality control reports completed by the Quality Control Technologist in the Radiology Department and were found to be within 2 percent of the selected kVp. The mAs selected varied with kVp in order to produce acceptable images on the TV monitor. At 40 kVp, 22 mAs was used and at 120 kVp, 0.5 mAs was used. The small focal spot size (0.6 mm) was chosen because of the greater radiographic detail achieved. The phantoms were placed on the table perpendicular to the anode-cathode angle to minimize the anode-heel effect. The collimator shutters were brought as close as possible to the object being imaged. To further minimize x-ray scatter from reaching the II, an extra sheet of lead (1 mm) was used. The centre was cut out to fit the lucite phantom. Two aluminum filters were used to absorb low energy x-rays. At 120 kVp the filter thickness was 2.54 cm while at 40 kVp the filter thickness was 0.521 cm. These filters absorbed the low energy x-rays that would contribute to the x-ray dose to

a patient with minimal degradation to the x-ray image. The unit was operated with the x-ray tube under and the II over the table (figure 3.3). The distance from the focal spot to the table was 32 cm and the distance from the table to the II was 61 cm.

3.3 Phantoms

3.3.1 Aluminum Stepwedge

A stepwedge (figure 3.4) was used to determine the attenuation coefficient of aluminum. Aluminum is an accepted bone substitute as its mass attenuation coefficient is similar to bone in the diagnostic energy range (see table 3.1). The stepwedge was 9.3 cm long, 0.98 cm wide and had 13 steps. The thickness of the steps, in centimeters, were as follows: 0.7005, 0.6498, 0.6025, 0.5549, 0.5085, 0.4598, 0.4108, 0.3603, 0.3099, 0.2582, 0.2126, 0.1595, 0.1084. The approximate thickness of a neonatal radius (2-3 mm) is within the range of step thicknesses. The density of aluminum is 2.6989 g/cm^3 (CRC Handbook of Chemistry and Physics).

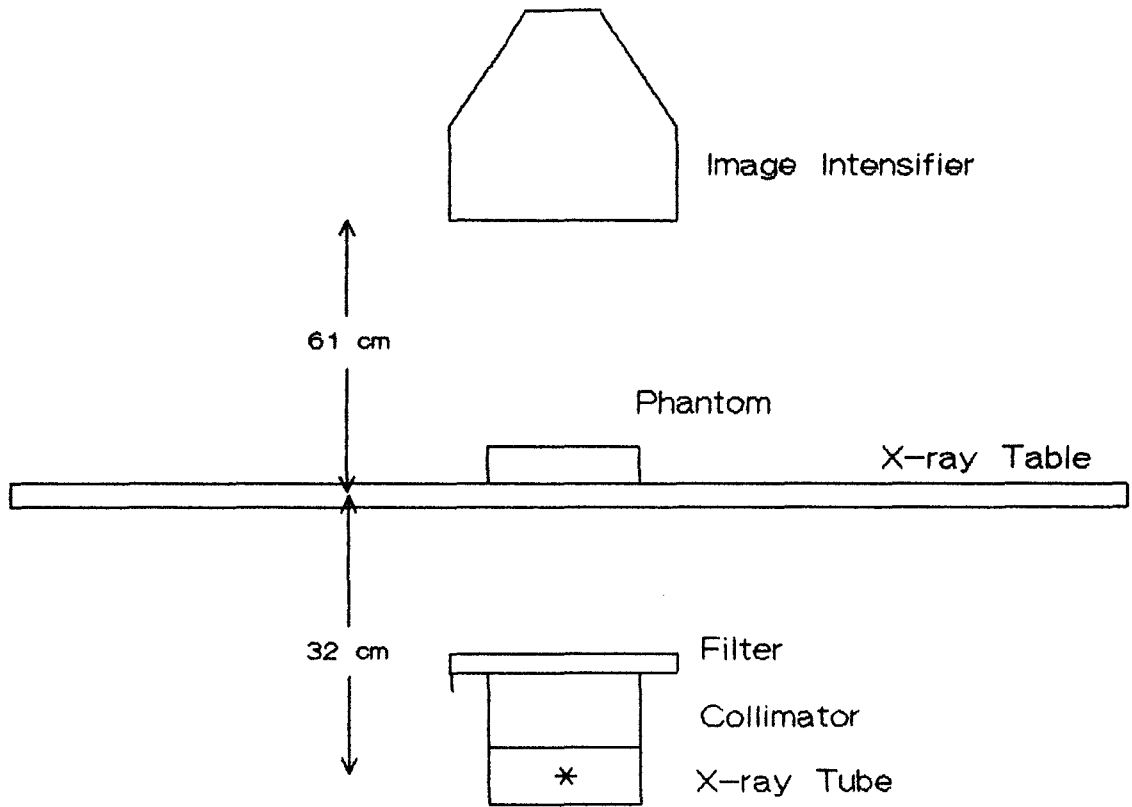


Figure 3.3 Experimental setup.

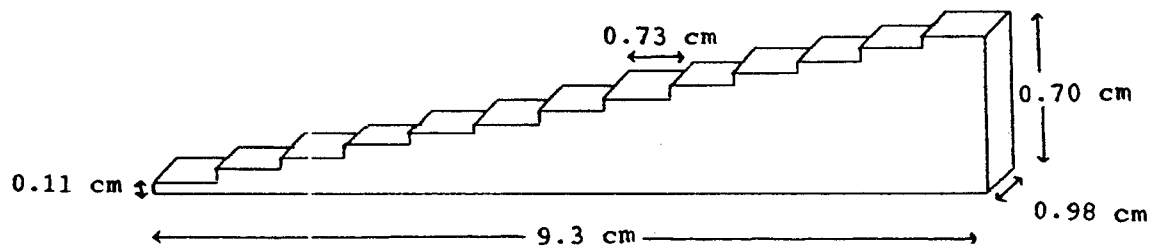


Figure 3.4 The aluminum stepwedge.

Energy (keV)	Aluminum	Bone	Water	Lucite	Soft Tissue
20	3.392	3.782	0.7958	0.5616	0.7498
30	1.115	1.267	0.3718	0.3006	0.3583
40	0.5630	0.6400	0.2668	0.2340	0.2605
50	0.3655	0.4121	0.2262	0.2069	0.2223
60	0.2763	0.3087	0.2055	0.1921	0.2027
80	0.2012	0.2215	0.1835	0.1750	0.1816
100	0.1701	0.1857	0.1707	0.1640	0.1691
150	0.1378	0.1492	0.1504	0.1456	0.1493

Table 3.1 Mass attenuation coefficients of bone, soft tissue and phantom materials as a function of photon energy.

3.3.2 Water Phantom

The water phantom was used to simulate the arm of a neonate. The aluminum stepwedge was placed in a 12 by 5 by 3.5 cm plastic container filled to the top with water. Water is an accepted soft tissue substitute since its mass attenuation coefficient is similar to that of soft tissue in the diagnostic energy range (see table 3.1).

3.3.3 Lucite Phantom

A lucite phantom was designed to replace the water phantom. A solid block of lucite with dimensions 10.15 cm by 2.31 cm and a thickness of 2.3122 cm with seven oval grooves of varying depths and widths was constructed at the Engineering Machine Shop, McMaster University. The varying thicknesses of lucite (0.9599, 1.2860, 1.4684, 1.6197, 1.7897, 1.8697, 2.0227 cm) below the grooves allowed the phantom to be used as a lucite stepwedge and were measured using a micrometer. The stepwedge was used when determining the attenuation coefficient of soft tissue. Lucite is an acceptable substitute for soft tissue given the similarity in their

mass attenuation coefficients in the diagnostic energy range (see table 3.1). The thickness of the lucite block was similar to the thickness of a neonatal arm (1.5-2.5 cm) as measured on neonatal x-rays taken at MUMC.

The mass of the lucite phantom was measured using the Sartorius scale (Model 244250008, Sartorius-Werke GMBH, Gottingen) located in the Nuclear Medicine Department at MUMC and was found to be 55.7935 g. The mass of the lucite phantom was then measured while suspended in a beaker of water and was found to be 9.4155 g. The difference between these two values would give the mass of the displaced water or the volume of the lucite in cm^3 . Therefore, the density of the lucite phantom could be calculated and was found to be 1.203 g/cm^3 . The accepted value is 1.19 g/cm^3 .

3.3.4 The Chicken Bones

Chicken bones were cleaned of soft tissue by boiling in water and were then soaked in a bath of acetone to remove any remaining fat. The bones were cut into 14 sections of varying mass. In order to simulate bone and tissue, sections of chicken bones were placed

in the grooves of the lucite phantom filled with water. The phantom was gently tapped until all visible air bubbles were eliminated. It was important to ensure that all air in the bones and grooves was removed as the mass attenuation coefficient of air is extremely different from that of either bone or tissue (Hubbell 1982).

3.4 Method

3.4.1 Acquiring the Digital Images

Preliminary images, Run #1, were acquired using the aluminum stepwedge and the water phantom with the purpose of obtaining mass attenuation coefficients for aluminum and water using equation 2.11. An image of the thick aluminum filter placed on the face of the collimator was acquired at 120 kVp. Any point in the image would be the initial x-ray beam intensity value, I_0 . The plastic container filled with water was placed upon the filter and an image was acquired giving the value of I at any point in the image. To determine the mass attenuation coefficient of aluminum, an image was then taken of the water filled container and the stepwedge. A similar set of images was acquired at 40

kVp.

The first image acquired for Run #2 was of the thick aluminum filter at 120 kVp. The filter was placed on the face of the collimator with the x-ray table in place as it would be when imaging a neonate. The lucite phantom containing 7 chicken bones was placed on the table and images were taken at 120 and 40 kVp. An image of the x-ray table, which replaced the thin aluminum filter, was acquired at 40 kVp. Images were also acquired of the stepwedge placed on the solid portion of the lucite phantom and the lucite phantom alone at both kVp settings.

Run #3 was a repeat of Run #2 including images of all 14 chicken bones.

Run #4 was a repeat of Run #3 using the extra lead sheet with the cut out to investigate the effect of extra collimation on the images. The lead sheet was used in all images acquired.

3.4.2 Accessing the Digital Images

The images of Run #1 and #2 were archived to magnetic tape by the Technicare Dr 960 High Speed Disk

System. The tapes were read off-line by a Digital PDP 11/34 computer using a proprietary operating system. The images were compressed to a 256 x 256 matrix and sent by serial link to a TygraPro 386 AT personal computer. The images were then accessed via a medical image display programme written in-house. The in-house programme, Display, was used to display individual pixel intensity values for any point in the image. Display had a function which could plot the pixel values along a slice of the image. The number of pixel values recorded was dependent on the size of the area being analyzed. The pixel values were recorded for each slice until the entire region of interest had been recorded. The images were displayed on a co-ordinate system so that each pixel value was represented by a set of x and y values. The co-ordinates were recorded along with the pixel values when analysing the images. Thus, accurate pixel values for I_0 were obtained when analysing the filter images.

A new method for accessing the digital information had to be developed due to mechanical breakdown of the magnetic tape drive. The Technicare

system had a resident program which computed mean pixel intensity values for a selected region of interest (ROI), either oval or rectangular, shown on the TV monitor. The ROI pixel count and standard deviation were also computed and were recorded along with the pixel values. A rectangular ROI was chosen for analysing the chicken bones and aluminum stepwedge, while an oval ROI was used for the lucite stepwedge. The ROI could be moved about the image via a joystick and was represented by a set of co-ordinates. This provided accurate analysis of the filter images similar to the Display program. Images in Run #3 and #4 were analyzed using this method.

3.4.3 Determination of Mass Attenuation Coefficients

The mass attenuation coefficients for aluminum were determined by plotting the following line for the aluminum stepwedge

$$\frac{1}{T_{Al}} \ln \left(\frac{I_o}{I} \right)_n = \left(\frac{\mu}{\rho} \right)_{Ln} \left(\frac{T_L}{T_{Al}} \right) + \left(\frac{\mu}{\rho} \right)_{Aln} \quad (3.1)$$

where n is the kVp setting and Al and L refer to

aluminum and lucite, respectively. Equation 3.1 is a rearrangement of equation 2.12 in the form of $y=mx+b$. The values of T_x , where x is Al or L, were determined by multiplying the density of x by the thickness of x . In Run #1, a mean pixel value for I was calculated at both kVp settings for each step of the aluminum stepwedge in the water phantom. Corresponding pixel values were determined from the filter images for the values of I_o . Similar calculations were done for the aluminum stepwedge in Run #2, #3 and #4. A linear regression of each data set gave the y -intercept and associated error of each line.

The mass attenuation coefficients for water in Run #1 were determined from equation 3.1 where water was used in place of lucite. The slope and error were obtained from the linear regression of each line at each kVp setting.

The mass attenuation coefficients for lucite were determined by plotting the following line

$$\ln \left(\frac{I_o}{I} \right)_n = \left(\frac{\mu}{\rho} \right)_{Ln} T_L \quad (3.2)$$

for the lucite stepwedge at each kVp setting. Equation 3.2 is a rearranged form of equation 2.11 and is in the form of $y=mx+b$. The equation was applied to Run #2, #3 and #4. A mean pixel value for I was calculated at both kVp settings for each step of the lucite stepwedge. Corresponding pixel values were determined from the filter images for the values of I_0 . The slope and associated error was determined from a linear regression of each data set.

3.4.4 Determination of BMD

The BMD for chicken bones was calculated using equation 2.14. The values for I_n and I_{on} , where n is 1 or 2, were obtained from images of the chicken bones in the lucite phantom and from filter images. The chicken bones were analysed separately by Run so that the corresponding mass attenuation coefficients could be used.

3.5 Single Photon Absorptionmetry (SPA)

The BMD of each chicken bone was also determined by the SPA method using a Norland Digital Bone

Densitometer, Model 278A (Norland Instruments, Fort Atkinson, Wisconsin). This was used as a comparison to the results obtained by the digital radiography method.

3.5.1 Calibration of Densitometer

The densitometer was calibrated with a bone and soft tissue phantom. This phantom is used clinically for calibration of the unit on a daily basis. The plastic block contains four bone phantoms of known BMD. The phantom is placed into the holder and scanned 16 times. An average BMD is calculated and displayed by the unit. A calibration factor is then calculated from the known value and the measured value and is entered into the unit.

3.5.2 Measurement of BMD

The chicken bones in the lucite phantom were positioned in the densitometer as shown in figure 3.5. The water bag normally used in patient measurements was not necessary as the lucite phantom was uniform in thickness. The densitometer calculates BMC in g/cm and bone width in cm. Each bone was measured five times and

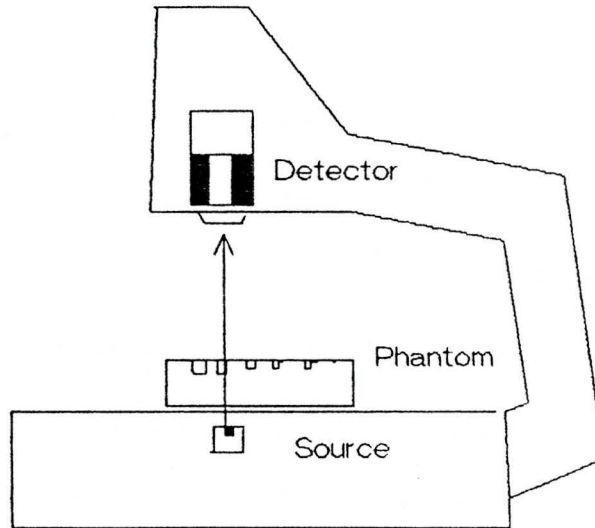


Figure 3.5 Experimental setup for the measurement of the chicken bones using SPA.

a mean value was calculated for BMC and bone width. The BMD (g/cm^2) was calculated for each bone using these results.

Chapter 4 Results and Discussion

4.1 SPA Results

The SPA measures of bone mineral densities for fourteen of the fifteen chicken bones are shown in table 4.1. The densitometer was unable to detect the smallest chicken bone. Each bone was measured five times and the mean value calculated.

4.2 Data Analysis

In this chapter, for all plots, each data point represents the mean value from a region of pixels which varies in size within different areas of the object on the digital image. Images of the aluminum stepwedge in Run #1 were analysed using 16 pixels per step. In Run #2, 108 to 133 pixels were analysed per step of the aluminum stepwedge. The edges of the wedge were not clearly visible on all steps due to the decrease in contrast between the larger steps and the background in

BONE	BONE MINERAL DENSITY g/cm ²
1	0.416 +/- 0.010
2	0.380 +/- 0.010
3	0.350 +/- 0.022
4	0.295 +/- 0.013
5	0.335 +/- 0.066
6	0.216 +/- 0.050
7	0.350 +/- 0.004
8	0.241 +/- 0.010
9	0.353 +/- 0.024
10	0.136 +/- 0.025
11	0.170 +/- 0.026
12	0.115 +/- 0.020
13	0.302 +/- 0.016
14	0.177 +/- 0.009

Table 4.1 Bone mineral densities of fourteen chicken bones using SPA.

the digital image. This resulted in different numbers of pixels per step even though the steps are all the same size. Each step of the lucite stepwedge was analysed using 93 to 210 pixels. The number of pixels used for the chicken bone images ranged from 135 to 553. In Run #3 and #4, 945 pixels were analysed per step of the aluminum stepwedge. A range of 781 to 2881 pixels were used for the images of the lucite stepwedge while the bone images were analysed using 273 to 1287 pixels.

The error bars of each data point represent one standard error. The error depended on the variation of pixel values in the region of interest analysed. The errors associated with each calculation of bone mineral density were obtained from a propagation of errors.

A table at the end of this chapter (table 4.5) summarizes the effective mass attenuation coefficients determined in the experimental runs.

4.3 Run #1

The results obtained from the stepwedge imaged at 120 kVp are shown in figure 4.1a. The slope of the line which gives the effective mass attenuation

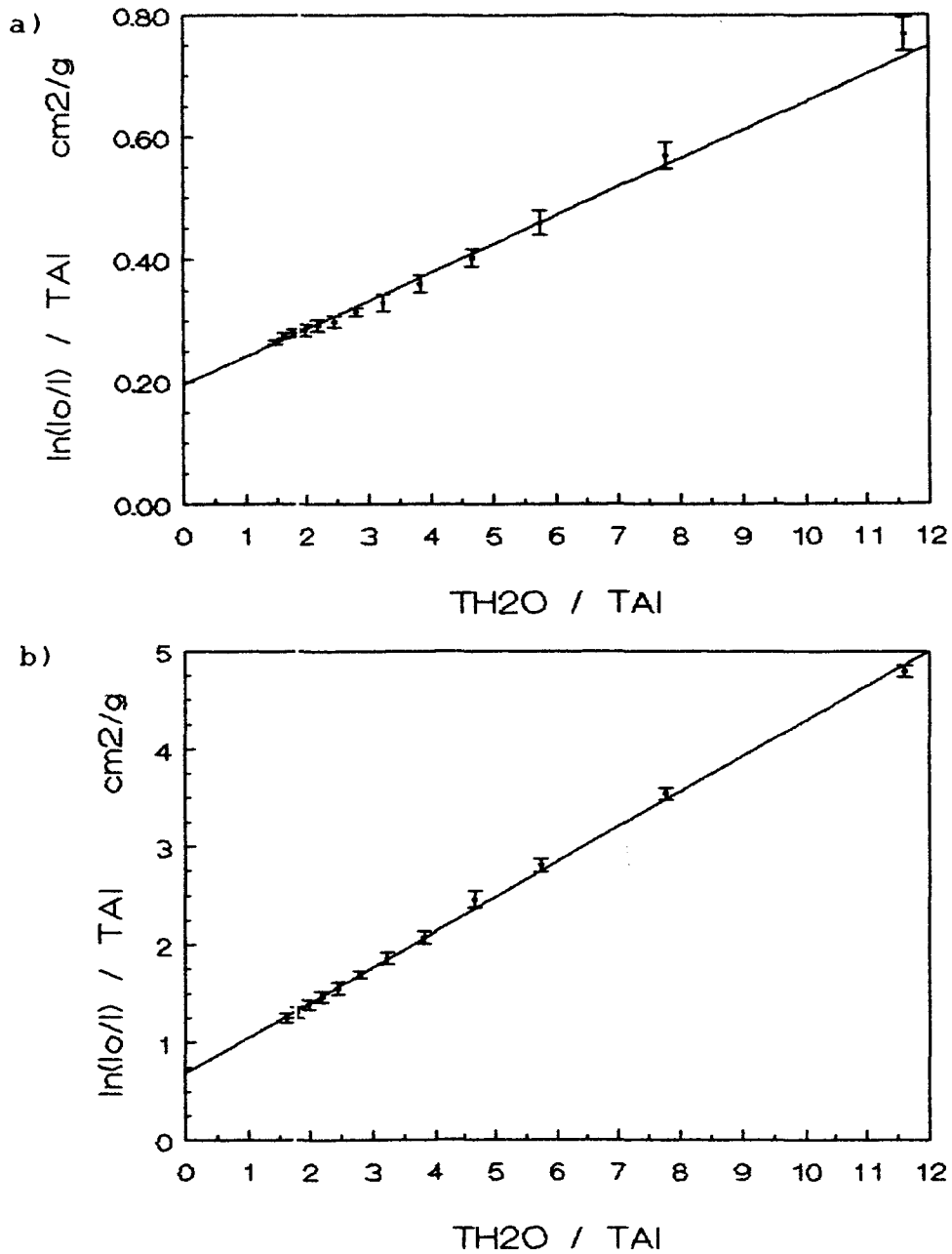


Figure 4.1 Determination of the effective mass attenuation coefficients of water and aluminum by linear regression of equation 3.1. The water phantom with the aluminum stepwedge are imaged at a) 120 kVp and b) 40 kVp.

coefficient (μ/ρ) of water was determined to be $0.462 \pm 0.002 \text{ cm}^2/\text{g}$ and the y-intercept which gives μ/ρ of aluminum is $0.195 \pm 0.004 \text{ cm}^2/\text{g}$. The value of μ/ρ for aluminum, denoted by the y-intercept, corresponded to coefficients determined for monoenergetic photons of 81.3 to 85.4 keV however μ/ρ for water did not fall within the expected range. The result was considered to be due to excessive scattering from water and aluminum at the higher kVp.

The results for the 40 kVp images were also plotted (figure 4.1b). When analysing the images, the thirteenth step was not discernible from the background on the computer monitor at 40 kVp and the results for only twelve steps are shown. The slope and y-intercept were $0.360 \pm 0.006 \text{ cm}^2/\text{g}$ and $0.688 \pm 0.027 \text{ cm}^2/\text{g}$ respectively. The measured values of the effective mass attenuation coefficients of aluminum and water were compared to the published values (Hubbell 1982) and correspond to coefficients determined for monoenergetic photons of approximately 30.6 to 31.3 keV and 36.1 to 37.4 keV respectively.

In order to better simulate the size of a

neonate's arm a new phantom made of lucite was constructed. The phantom had steps of varying thickness so that it could be used as a stepwedge. This enabled the measurement of the mass attenuation coefficients for lucite.

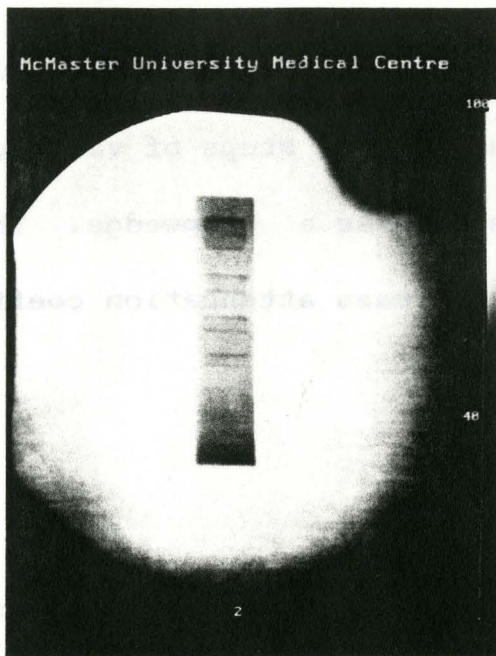
4.4 Run #2

The data obtained from Run #2 was analysed and bone mineral densities were determined for six out of the seven chicken bones imaged. The image of bone 1 at 40 kVp could not be analysed as the pixel values were equal to zero. Digital images of the chicken bones in the lucite phantom, as viewed in Display, are shown in figure 4.2 at 120 and 40 kVp. Digital images of the aluminum and lucite stepwedges were analysed and attenuation coefficients calculated.

Figures 4.3a and 4.3b show the results for the stepwedge images at 120 kVp and 40 kVp respectively. The y-intercept of figure 4.3a gives a μ/ρ value for aluminum of $0.211 \pm 0.006 \text{ cm}^2/\text{g}$. For figure 4.3b μ/ρ is $0.975 \pm 0.003 \text{ cm}^2/\text{g}$.

The lucite stepwedge was used to determine μ/ρ

a)



b)



4.2 Digital images of the chicken bones in the lucite phantom. The images were acquired at a) 120 kVp and b) 40 kVp.

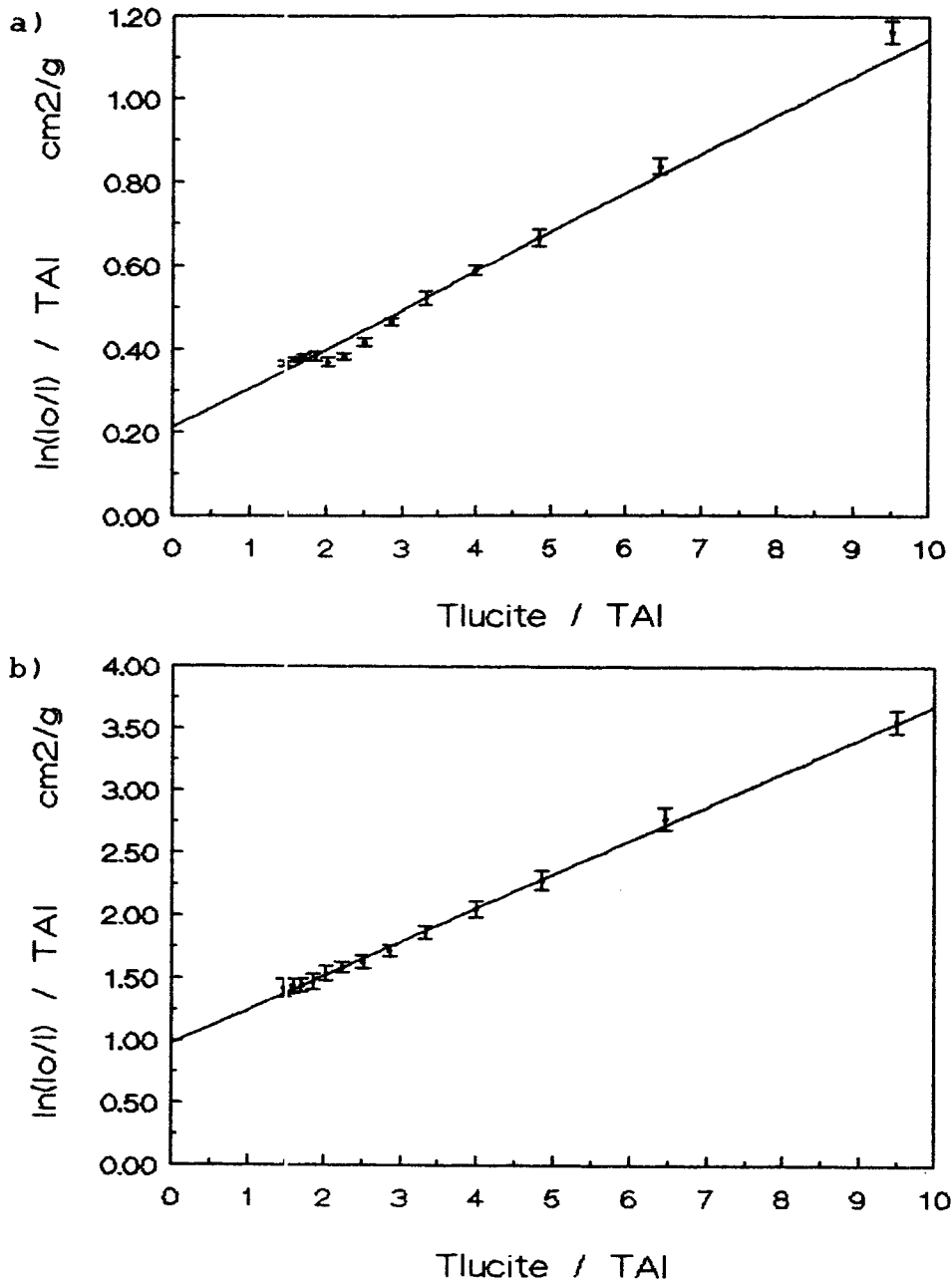


Figure 4.3 Determination of the effective mass attenuation coefficients of lucite and aluminum by linear regression of equation 3.1. The lucite phantom and aluminum stepwedge were imaged at a) 120 kVp and b) 40 kVp.

for lucite. The slope of the line for the lucite stepwedge imaged at 120 kVp (figure 4.4a) was $0.138 \pm 0.002 \text{ cm}^2/\text{g}$. At 40 kVp, μ/ρ for the lucite stepwedge was $0.283 \pm 0.006 \text{ cm}^2/\text{g}$ (figure 4.4b).

Bone mineral densities for 6 out of 7 chicken bones imaged were calculated, as per section 3.4.4, using the above mass attenuation coefficients (see table 4.2).

The bone mineral densities obtained by digital radiography were plotted in figure 4.5 against the results obtained from single photon absorptiometry. The smallest bone was not able to be measured by SPA and was therefore excluded from the plot. The correlation coefficient for the plot was 0.673. Though the values of BMD are different, it is clear that a relationship exists between the two methods.

More chicken bones were collected for subsequent analyses in which the effect of reducing the influence of scatter by increasing collimation was investigated.

4.5 Run #3

Bone mineral densities were determined for

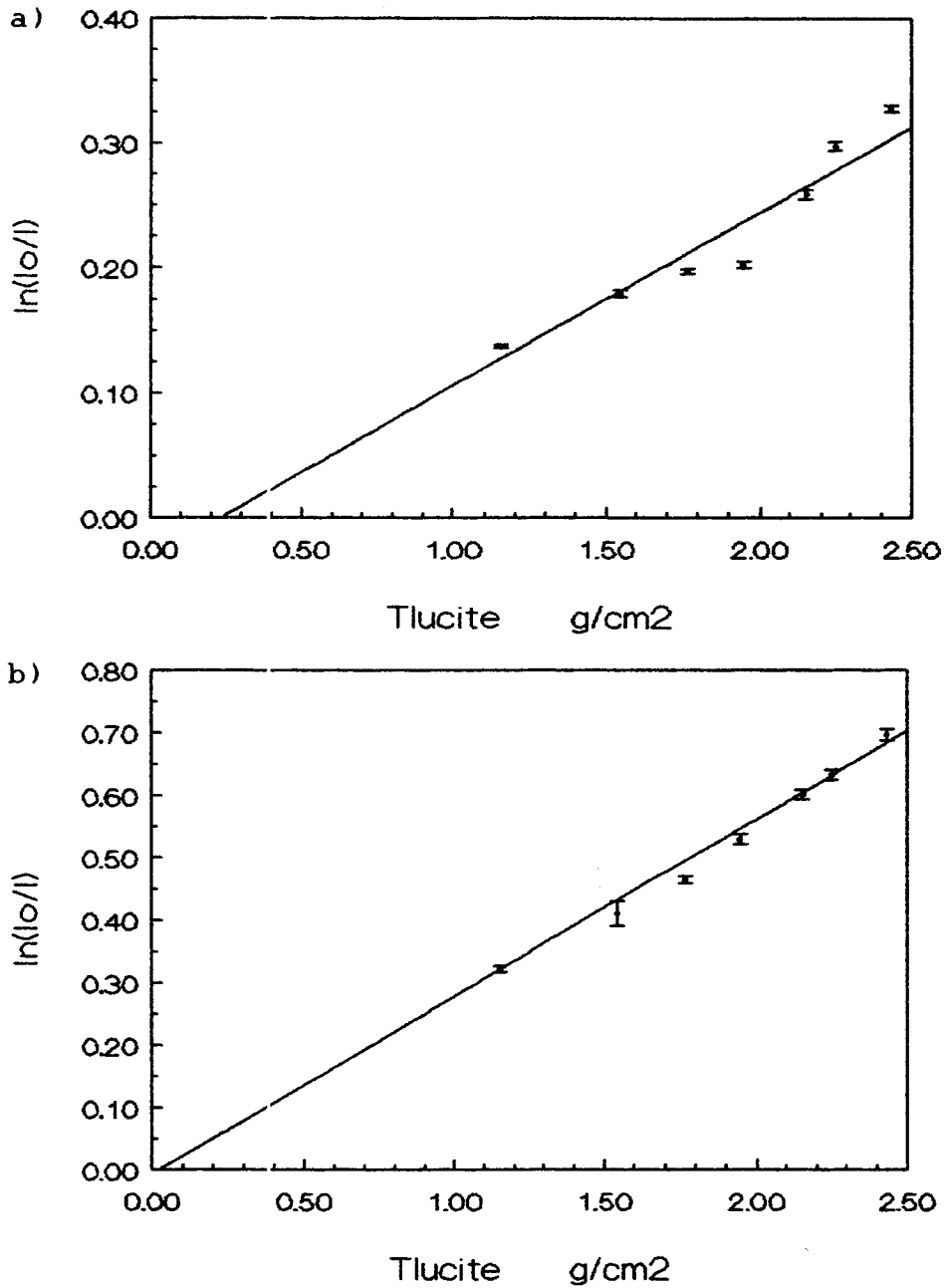


Figure 4.4 Determination of the effective mass attenuation coefficient of lucite by linear regression of equation 3.2. The lucite stepwedge was imaged at a) 120 kVp and b) 40 kVp.

BONE	NUMBER OF PIXELS	BONE MINERAL DENSITY g/cm ²
1	-	-
2	228	1.808 +/- 0.091
3	228	1.677 +/- 0.065
4	190	1.557 +/- 0.061
5	176	1.479 +/- 0.060
6	168	1.516 +/- 0.061
7	135	0.827 +/- 0.033

Table 4.2 Bone mineral densities of six chicken bones using digital radiography.

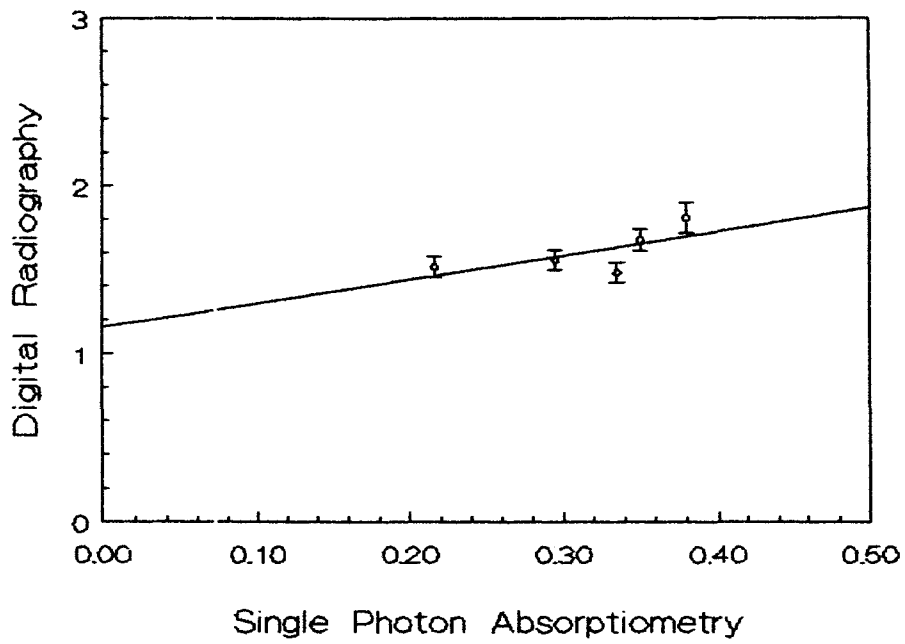


Figure 4.5 Comparison of the bone mineral densities of five chicken bones obtained by digital radiography and SPA.

thirteen of the fourteen chicken bones imaged with additional collimation. Bone 1 was not distinguishable from the background at 40 kVp and could not be analysed. Stepwedge images were analysed and attenuation coefficients for aluminum and lucite calculated.

Figures 4.6a and 4.6b show the results for the stepwedge images at 120 kVp and 40 kVp, respectively. The y-intercept of figure 4.6a gives a μ/ρ value for aluminum of $0.205 \pm 0.002 \text{ cm}^2/\text{g}$ and μ/ρ for aluminum from figure 4.6b is $0.484 \pm 0.029 \text{ cm}^2/\text{g}$.

The slope of the line for the lucite stepwedge imaged at 120 kVp (figure 4.7a) was $0.131 \pm 0.002 \text{ cm}^2/\text{g}$. At 40 kVp, μ/ρ for the lucite stepwedge was $0.233 \pm 0.003 \text{ cm}^2/\text{g}$ (figure 4.7b). The variation of pixel values for each data point was less than in Run #2 which is evident from the smaller error bars. This was thought to be a result of the improved collimation.

The bone mineral densities of the thirteen bones, table 4.3 were calculated using the measured mass attenuation coefficients and the values were plotted against the SPA results (figure 4.8). The large errors associated with four of the data points were most likely

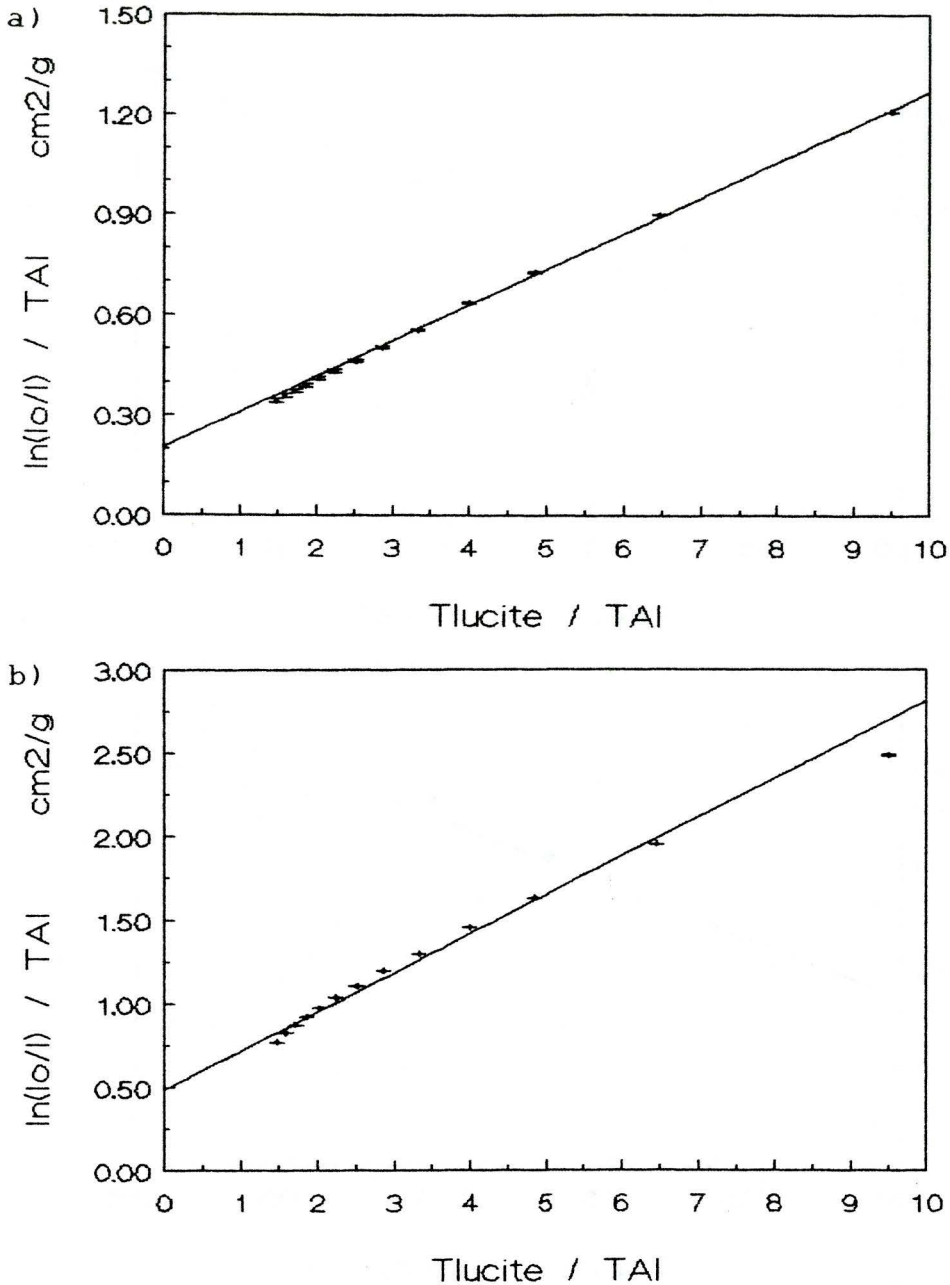


Figure 4.6 Determination of the effective mass attenuation coefficients of lucite and aluminum by linear regression of equation 3.1. The lucite phantom and aluminum stepwedge were imaged at a) 120 kVp and b) 40 kVp.

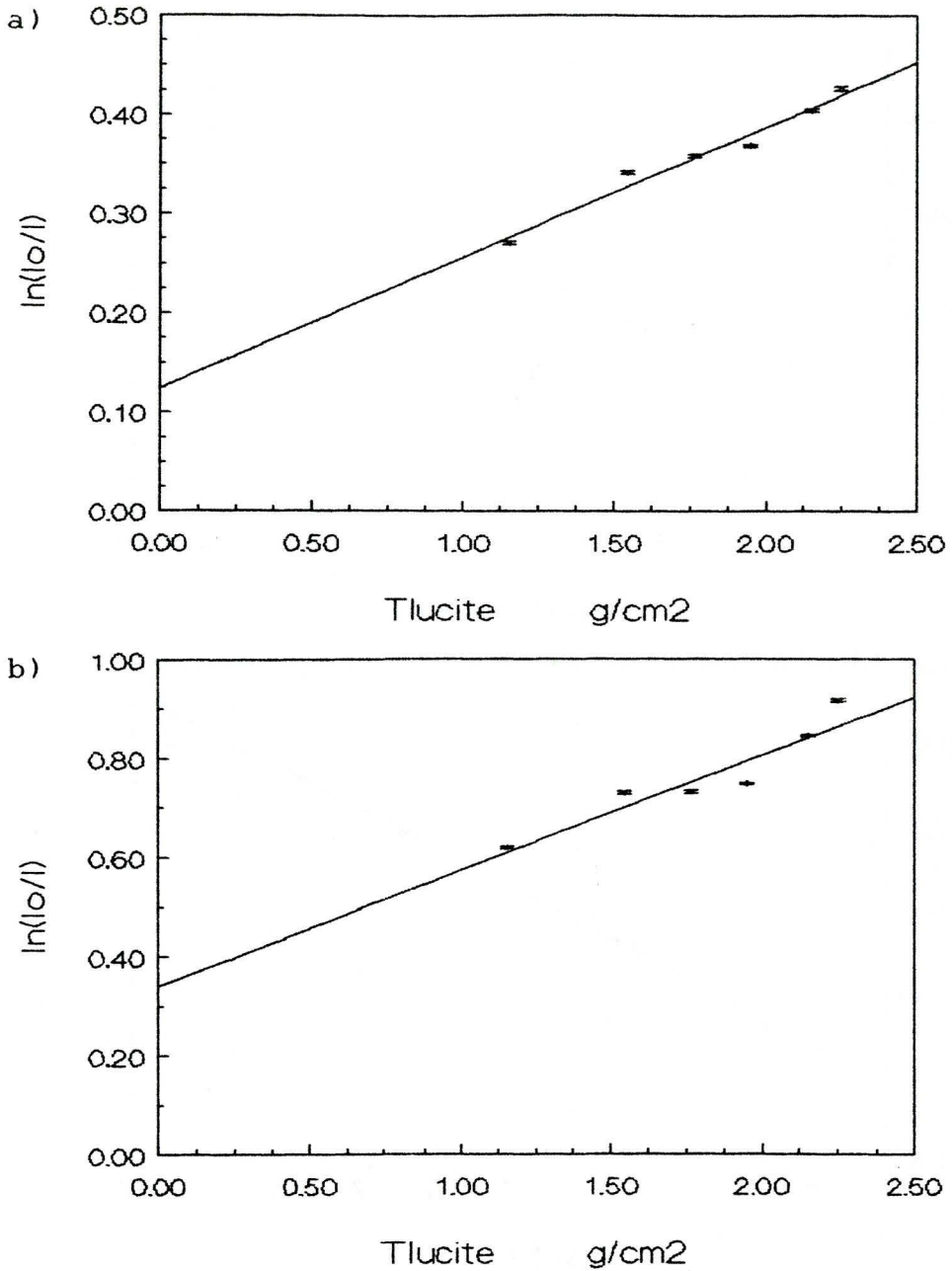


Figure 4.7 Determination of the effective mass attenuation coefficients of lucite by linear regression of equation 3.2. The lucite stepwedge was imaged at a) 120 kVp and b) 40 kVp.

BONE	NUMBER OF PIXELS	BONE MINERAL DENSITY g/cm ²
1	-	-
2	897	3.352 +/- 0.252
3	697	1.781 +/- 0.268
4	533	1.294 +/- 0.195
5	369	1.406 +/- 0.212
6	369	1.282 +/- 0.194
7	1073	2.329 +/- 0.705
8	697	1.675 +/- 0.511
9	615	1.812 +/- 0.553
10	369	0.896 +/- 0.285
11	287	0.684 +/- 0.224
12	273	0.797 +/- 0.257
13	645	1.600 +/- 0.491
14	287	0.796 +/- 0.258

Table 4.3 Bone mineral densities of thirteen chicken bones using digital radiography.

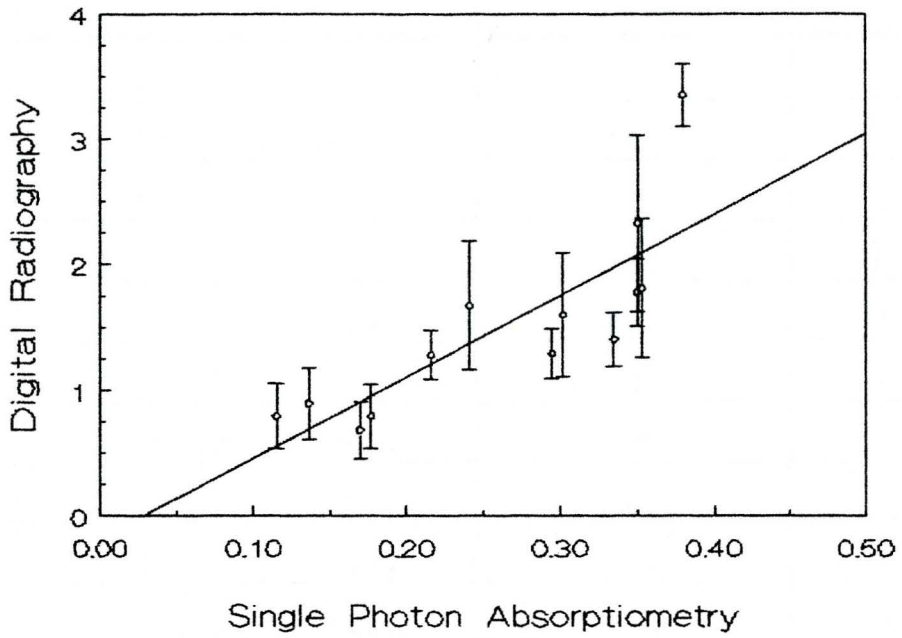


Figure 4.8 Comparison of the bone mineral densities of thirteen chicken bones obtained by digital radiography and SPA.

due to scattering in the larger bones. Within the calculated errors, all but three of the data points intersected the regression line. The correlation coefficient was 0.810. The improved agreement of BMD values from digital radiography with SPA was believed to be a direct result of improved collimation.

The values of BMD determined by digital radiography may be further improved by use of additional collimation. The lead sheet with the cutout for the phantoms was used and investigated in the following run.

4.6 Run #4

Bone mineral densities were determined for fourteen chicken bones. Images of the stepwedges were analysed and attenuation coefficients for aluminum and lucite calculated.

Figures 4.9a and 4.9b show the results for the stepwedge images at 120 kVp and 40 kVp, respectively. The y-intercept of figure 4.9a, which gives a value for μ/ρ of aluminum, is $0.052 \pm 0.001 \text{ cm}^2/\text{g}$, whereas in figure 4.9b the y-intercept is $-0.277 \pm 0.001 \text{ cm}^2/\text{g}$. The attenuation coefficient of aluminum is much lower in

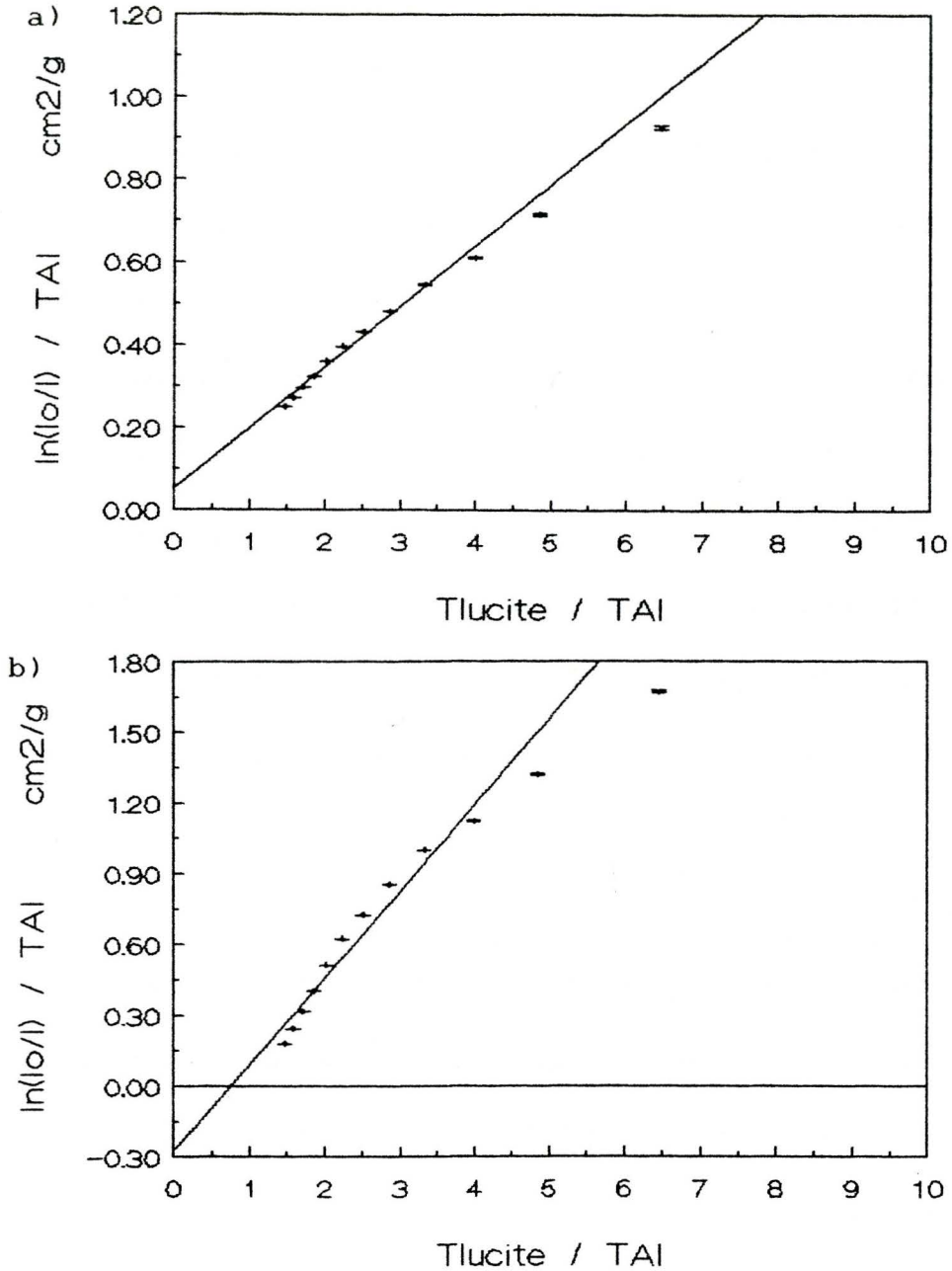


Figure 4.9 Determination of the effective mass attenuation coefficients of lucite and aluminum by linear regression of equation 3.1. The lucite phantom and aluminum stepwedge were imaged at a) 120 kVp and b) 40 kVp.

this case than previously determined. The data points in figures 4.9a and 4.9b decrease rapidly at Tlucite / TAL values less than three. This is likely due to the absorption of scattered radiation which previously reached the image intensifier. The slope of the line for the lucite stepwedge imaged at 120 kVp (figure 4.10a) was $0.133 \pm 0.002 \text{ cm}^2/\text{g}$. At 40 kVp, μ/ρ for the lucite stepwedge was $0.273 \pm 0.002 \text{ cm}^2/\text{g}$ (figure 4.10b).

The bone mineral densities of the fourteen bones were calculated using the measured mass attenuation coefficients (see table 4.4). These values were plotted against the SPA results (figure 4.11). The correlation coefficient was 0.424. The values of bone mineral density obtained from the digital radiography method are in better agreement with the values obtained from SPA than in Run #3. This is believed to be a direct result of the added collimation. The decrease in the error of each data point is also believed to be a result of the added collimation as the error depends on the variation in values between pixels.

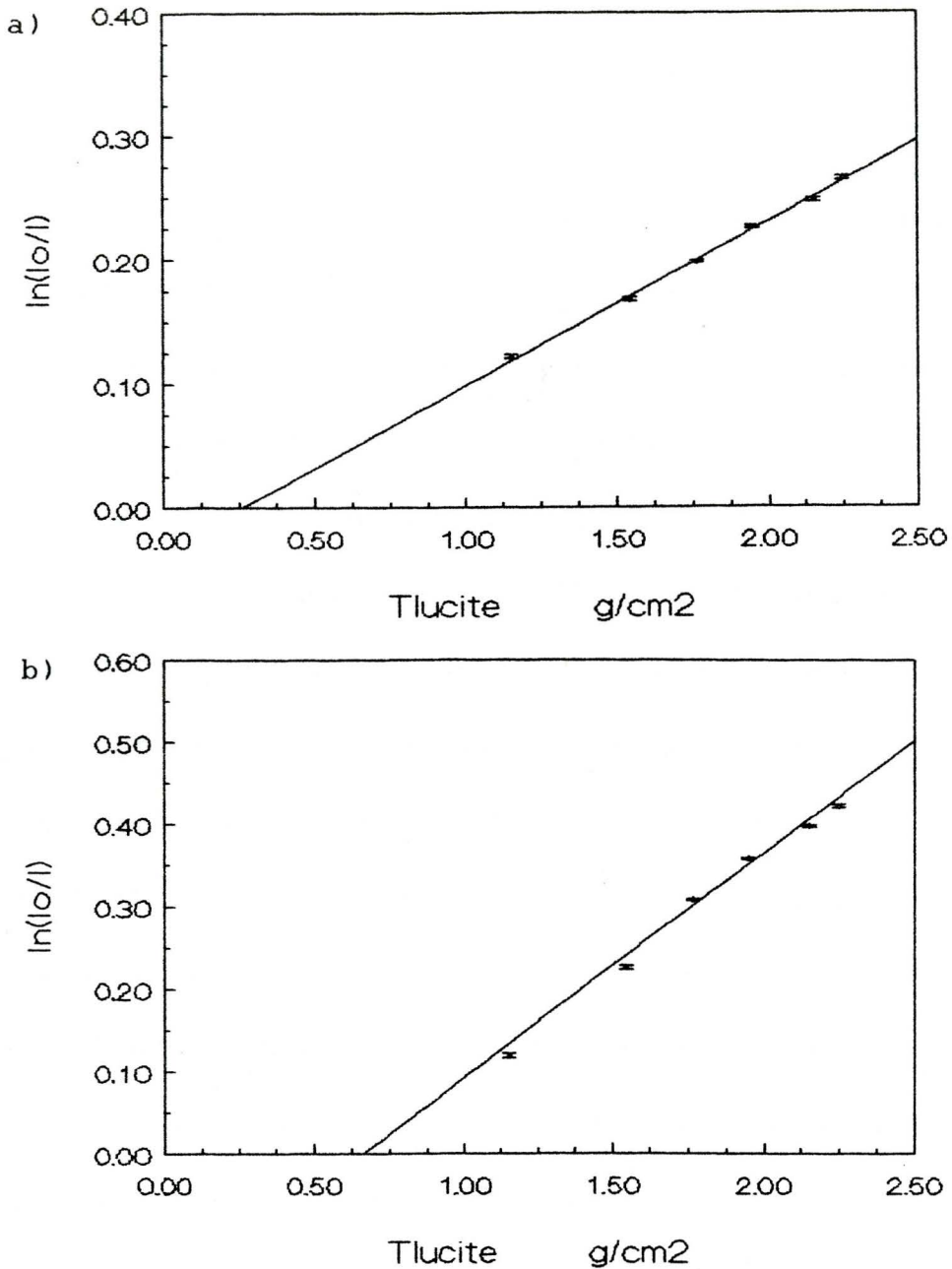


Figure 4.10 Determination of the effective mass attenuation coefficients of lucite by linear regression of equation 3.2. The lucite stepwedge was imaged at a) 120 kVp and b) 40 kVp.

BONE	NUMBER OF PIXELS	BONE MINERAL DENSITY g/cm ²
1	1287	0.774 +/- 0.035
2	897	0.502 +/- 0.036
3	697	0.323 +/- 0.036
4	533	0.349 +/- 0.039
5	369	0.372 +/- 0.040
6	369	0.383 +/- 0.039
7	1073	0.759 +/- 0.035
8	697	0.517 +/- 0.035
9	615	0.327 +/- 0.035
10	369	0.387 +/- 0.036
11	287	0.361 +/- 0.036
12	273	0.377 +/- 0.039
13	645	0.722 +/- 0.035
14	287	0.453 +/- 0.038

Table 4.4 Bone mineral densities of fourteen chicken bones using digital radiography.

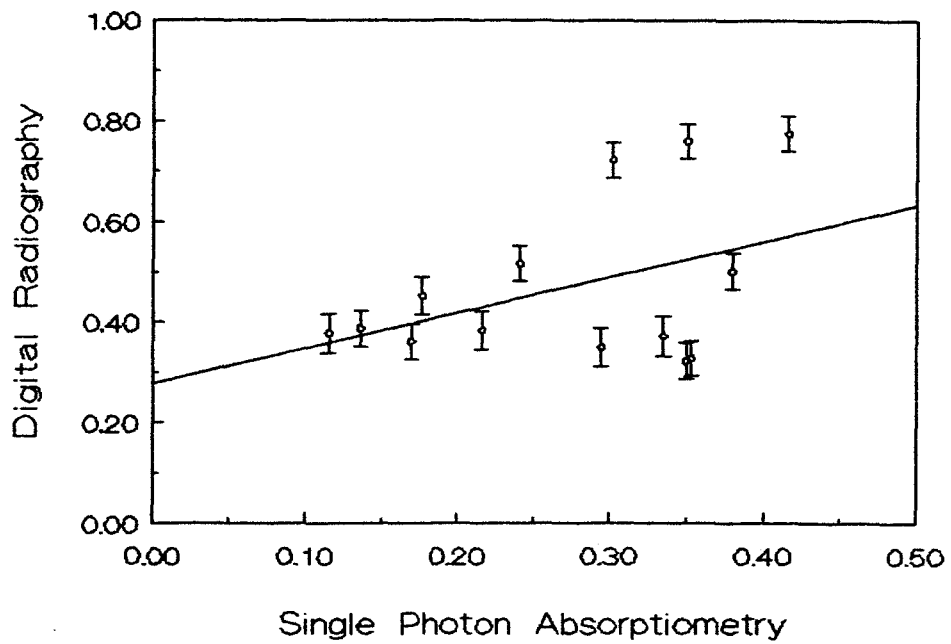


Figure 4.11 Comparison of the bone mineral densities of thirteen chicken bones obtained by digital radiography and SPA.

Run	Effective mass attenuation coefficients (cm ² /g)					
	Aluminum		Lucite		Water	
	120 kVp	40 kVp	120 kVp	40 kVp	120 kVp	40 kVp
1	0.195 ± 0.004	0.688 ± 0.027	-	-	0.462 ± 0.002	0.360 ± 0.006
2	0.211 ± 0.006	0.975 ± 0.003	0.138 ± 0.002	0.283 ± 0.006	-	-
3	0.205 ± 0.002	0.484 ± 0.029	0.131 ± 0.002	0.233 ± 0.003	-	-
4	0.052 ± 0.001	- 0.277 ± 0.001	0.133 ± 0.002	0.273 ± 0.002	-	-

Table 4.5 Summary of effective mass attenuation coefficients determined.

Chapter 5 Summary

A procedure to determine bone mineral density using digital radiography was developed. Digital radiographic images were acquired at 120 and 40 kVp using a digital angiography unit. The digital information from phantom images of aluminum, water and lucite phantoms and chicken bones was accessed and used directly. Effective mass attenuation coefficients of water, aluminum and lucite were determined at each kVp setting. These values and the digital information from the chicken bone images were used in subsequent calculations of bone mineral density.

Preliminary results from Run #1 and #2 showed that mass attenuation coefficients could be calculated and used to determine bone mineral density of sections of chicken bones. Due to a breakdown of the magnetic tape drive of the digital angiography unit, analysis of subsequent experiments were accomplished using a

different method.

Results from Run #3 showed an improvement in correlation of BMD values determined from digital radiography and SPA. This was believed to be due to improved collimation.

In run #4 there was an obvious improvement in the comparison between absolute BMD values measured by digital radiography and SPA. This was believed to be due to the use of additional collimation.

Overall, it has been shown that digital radiography can be used to measure bone mineral density. The BMD values obtained using this technique were similar to those obtained using SPA. The difference in these values could be due to the differences in image acquisition. SPA images a single thin slice whereas digital radiography images a larger area of bone. Therefore the digital radiography values could be affected by inhomogeneities in BMD over the areas of bones imaged.

The validity of the digital radiography method could be further tested by imaging homogeneous, cylindrical bone or aluminum phantoms and comparing the

results with SPA. Measurements of radius bone mineral density could then be made on normal subjects.

BIBLIOGRAPHY

Barden, H.S., Mazess, R.B., 1988 "Bone densitometry in infants." J Pediatr 113 pp 172-177.

Cameron, J.R., Sorenson, J., 1963 "Measurement of bone mineral in vivo: An improved method." Science 142 pp 230-236.

Greer, F.R., Lane, J., Weiner, S., Mazess, R.B., 1983 "An accurate and reproducible absorptiometric technique for determining bone mineral content in newborn infants." Pediatr Res 17 pp 259-262.

Hansen, J.W., 1988 "Proc. Symp. Asses. Bone Mineral Infants." J Pediatr 113 p 199.

Hawkes, D.J., Doran, M., McIntosh, N., Lyon, A., Theodoridou, A., Williams, J.E., 1987 "Development of a digital radiographic technique to measure bone mineral in neonates." Sixth Int. Workshop Bone Soft Tissue Densitometry, Buxton, p 76.

Hubbell, J.H., 1982 "Photon mass attenuation

coefficients from 1 keV to 20 MeV." Int J Appl Radait Isot 33 pp 1269-1290.

James, J.R., Truscott, J., Congdon, P.J., Horsman, A., 1986 "Measurement of bone mineral content in the human fetus by photon absorptiometry." Early Hum Dev 13 pp 169-181.

Koo, W.K., Oestreich, A., Tsang, R., et al, 1986 "Natural history of rickets and fractures in very low birth weight (VLBW) infants during infancy, abstracted." J Bone Min Res 1 p 123.

Lyon, A.J., Hawkes, D.J., Doran, M., McIntosh, N., Chan, F., 1989 "Bone mineralisation in preterm infants measured by dual energy radiographic densitometry." Arch Dis Child 64 pp 919-923.

Steichen, J.J., 1988 "Proc. Symp. Asses. Bone Mineral Infants." J Pediatr 113 p 196.

Steichen, J.J., Asch, P.A., Tsang, R.C., 1988 "Bone mineral content measurement in small infants by single-photon absorptiometry: Current methodologic issues." J Pediatr 113 pp 181-187.

Steichen, J.J., Edwards, N.K., Tsang, R.C., 1978 "Adaption of direct photon absorptiometry for

measurement of bone mineral content in small infants."

Am J Roentgenol 131 pp 539-543.

Steichen, J.J., Gratton, T.L., Tsang, R.C., 1980
"Osteopenia of prematurity: The cause and possible
Treatment." J Pediatr 96 pp 528-534.

Tyson, J.E., Maravilla, A., Lasky, R.E., Cope, F.A.,
Mize, C.E., 1983 "Measurement of bone mineral content of
preterm infants." Am J Dis Child 137 pp 735-737.

Vymeister, N.R., Linkhart, T.A., Hay, S., Baylink, D.J.,
Ghosh, B., 1987 "Measurement of bone mineral content in
the term and preterm infant." Am J Dis Child 141 pp
506-510.

Vymeister, N.R., Linkhart, T.A., 1988 "Measurement of
humerous and radius bone mineral content in the term and
preterm infant." J Pediatr 113 pp 188-195.

873300004